Chemical Engineering Journal 411 (2021) 128416

Contents lists available at ScienceDirect

Chemical Engineering Journal

journal homepage: www.elsevier.com/locate/cej

Using redox electrolytes to extend the charge storage capacity in an aqueous hybrid ion battery

S.T. Senthilkumar [a,b,*], Jeong-Sun Park [a,c], Rebeca Marcilla [b], Jesus Palma [b], Youngsik Kim [a,c,*]

[a] School of Energy & Chemical Engineering, Ulsan National Institute of Science and Technology (UNIST), Ulsan 689-798, Republic of Korea
[b] Electrochemical Processes Unit, IMDEA Energy, Avda. Ramón de La Sagra 3, 28935 Móstoles, Madrid, Spain
[c] Energy Materials and Devices Lab, 4TOONE Corporation, UNIST-gil 50, Ulsan 689-798, Republic of Korea

ARTICLE INFO

Keywords:
Hybrid ion battery
Redox electrolyte
Nickelhexacyanoferrate
Sodium ferrocyanide
4-Hydroxy-2
2,6,6-Tetramethylpiperidine-1-oxyl

ABSTRACT

Aqueous hybrid Zn^{2+}/Na^{+} ion batteries (AHZSIBs) have gained considerable attention for stationary energy storage applications because of their outstanding safety, sustainability, abundance, and low raw material costs. However, the low capacity values (<100 mAh/g) of the Na^{+} ion deinsertion/insertion cathodes limit the overall capacity storage of AHZSIBs. Herein, we propose a novel concept to extend the charge storage performance of AHZSIBs using electrolyte with redox characteristics. The benefits of using redox aqueous electrolytes such as 4-hydroxy-2,2,6,6-tetramethylpiperidine-1-oxyl (TEMPOL) and sodium ferrocyanide ($Na_4[Fe(CN)_6]$) were investigated in an AHZSB, which consists of Zn metal as an anode and sodium nickel hexacyanoferrate (Na-NiHCF) as the Na^{+} deinsertion/insertion cathode. The proposed AHZSB using $Na_4[Fe(CN)_6]$ redox electrolyte provided a capacity (144 mAh/g) that was ~2.94 times higher than AHZSIB using a conventional Na_2SO_4 electrolyte (49 mAh/g). This capacity enhancement emanated from the faradaic contribution of the $Fe^{2+}(CN)_6^{4-}/Fe^{3+}(CN)_6^{3-}$ redox pair present in the electrolyte and Fe^{2+}/Fe^{3+} redox pair in the lattice of Na-NiHCF. In addition, the TEMPOL-based redox electrolyte also improved the capacity (from 49 to 120 mAh/g) through the combined faradaic contribution of the TEMPOL/$TEMPOL^{+}$ redox pair dissolved in the electrolyte and the Fe^{2+}/Fe^{3+} redox pair in the Na-NiHCF lattice. These results confirm the competence of the redox electrolyte in AHZSIB in enhancing the charge storage capacity. We anticipate that this proof-of-concept study will provide a new direction for developing high-capacity storage AHZSIBs. More importantly, this approach can be used in any aqueous/non-aqueous batteries.

1. Introduction

Carbon dioxide (CO_2) is the leading cause of global warming and climate change. Nearly 80% of CO_2 is produced by coal-based power plants and fossil fuel-based (e.g., oil and gas) transport sectors. Hence, most countries are now shutting down coal-based power plants and reducing the use of combustion engine vehicles by utilizing renewable energy technologies (i.e., solar and wind power) and implementing electric vehicles/transports (i.e., cars, trains, trucks, and buses), respectively. Therefore, energy storage systems have become a critical element in ensuring the effective deployment of renewable energy technology and the development of electric vehicles. Currently, lead-acid batteries (LABs) and Li-ion batteries (LIBs) are the most widely used and well-known electrochemical energy storage systems. LIBs are an attractive candidate for high energy density charge storage (150–200 Wh/kg) but are costly (~250 USD per kWh), and present safety issues; these factors hinder their ability from scaling up for large-scale energy storage applications [1,2]. In contrast, LABs are low-cost (~170 USD per kWh) and are more appropriate for large-scale energy storage applications because they rely on aqueous electrolytes and simple cell assembly technology. Nevertheless, the toxicity of lead in LABs, their limited energy density (30–50 Wh/kg), and their short life span (<500 cycles) have created a demand for battery experts to develop less hazardous aqueous rechargeable batteries with lower costs (~100 USD per kW/h), a higher energy density, and longer cycle life [2–4].

Recently, a new concept of an aqueous hybrid Zn/Na-ion battery (AHZSIB) has been demonstrated through combining a metallic Zn anode and a Na^{+} ion deinsertion/insertion cathode [5–8]. AHZSIBs are low-cost, non-flammable, and environmentally friendly, and these features could make them an attractive contender for stationary energy

* Corresponding authors.
E-mail addresses: senkumphy@gmail.com (S.T. Senthilkumar), ykim@unist.ac.kr (Y. Kim).

https://doi.org/10.1016/j.cej.2021.128416
Received 30 September 2020; Received in revised form 6 December 2020; Accepted 1 January 2021
Available online 8 January 2021
1385-8947/© 2021 The Author(s). Published by Elsevier B.V. This is an open access article under the CC BY-NC-ND license (http://creativecommons.org/licenses/by-nc-nd/4.0/).

storage applications over LIBs and LABs. In general, Zn can offer a high capacity (819 mAh/g) and low redox (Zn/Zn^{2+}) potential (−0.78 V vs SHE (**S**tandard **H**ydrogen **E**lectrode), which are important factors for boosting the energy density of AHZSIB. In addition, Zn is a low-cost and safer metal than Li, Na, and K for use in aqueous-based batteries. Thus far, $Na_{0.44}MnO_2$ [9], $Na_4Mn_9O_{18}$ [10], $Na_2NiFe(CN)_6$ [6], $Na_2CuFe(CN)_6$) [7], sodium iron hexacyanoferrate [5,8], $Na_3V_2(PO_4)_3$ [11–13], and $Na_3V_2(PO4)_2F_3$ [14,15] have been as studied Na^+ ion insertion/deinsertion cathodes in AHZSIBs. Regrettably, these Na^+ ion insertion/deinsertion cathodes delivered low capacities (50–100 mAh/g) and thus resulted in low energy density AHZSIBs. Therefore, it is essential to create new high-capacity Na^+ ion insertion/deinsertion cathodes for AHZSIB or to develop a novel strategy to elevate the capacity of the cathode part in AHZSIB.

Previous studies on supercapacitors have reported that compared to the conventional electrolyte, the use of a redox electrolyte (e.g., KI, $K_4[Fe(CN)_6]/K_3[Fe(CN)_6]$, $BiBr_3$, hydroquinone and *para*-Benzoquinone) [16–21] significantly enhances the capacitance of the electrode materials by providing redox species involved in the redox reaction at the electrolyte–electrode interfaces. Similarly, the potential of redox electrolytes (e.g., $K_3[Fe(CN)_6]/K_4[Fe(CN)_6]$ and $Na_4[Fe(CN)_6]$) with Na^+ ion insertion/deinsertion electrode materials have also been realized in redox flow batteries [22,23] and hybrid electrolyte-based battery [24] through attaining an enhanced charge storage capacity. Based on these reports, in this study, instead of developing a new high-capacity Na^+ ion deinsertion/insertion cathode, we propose the replacement of the conventional aqueous electrolyte with a suitable aqueous redox electrolyte as a simple strategy to boost the overall charge storage capacity of the cathode in an AHZSIB. This proposed approach can effectively combine the faradic capacity of electrolyte dissolved redox species with a capacity of Na^+ ion insertion/deinsertion cathode. In our assembled AHZSIB, Zn metal foil behaves as an anode in a $Na_2SO_4/ZnSO_4$ electrolyte, and sodium nickel hexacyanoferrate (Na-NiHCF) serves as the Na^+ ion insertion/deinsertion cathode in a sodium ferrocyanide ($Na_4[Fe(CN)_6]$) redox electrolyte or hydroxy-2,2,6,6-tetramethylpiperidine-1-oxyl (TEMPOL)/Na_2SO_4 redox electrolyte. The redox pair, $Fe^{2+}(CN)_6^{4-}/Fe^{3+}(CN)_6^{3-}$ dissolved in the $Na_4[Fe(CN)_6]$ redox electrolyte and TEMPOL/$TEMPOL^+$ dissolved in the TEMPOL/Na_2SO_4 redox electrolyte enhanced the capacity (energy density) of AHZSIB to 144 mAh/g (165 Wh/kg) and 120 mAh/g (165 Wh/kg), respectively. However, because of the absence of redox species, the conventional Na_2SO_4 electrolyte used in AHZSIB exhibited a lower capacity (energy density) of 49 mAh/g (64 Wh/kg). Notably, compared to TEMPOL/$TEMPOL^+$, the $Fe^{2+}(CN)_6^{4-}/Fe^{3+}(CN)_6^{3}$ pair containing the $Na_4[Fe(CN)_6]$ redox electrolyte acquired a 100% capacity retention even after several repeated charge and discharge cycles, owing to its excellent electrochemical stability. This comprehensive study highlights the feasibility of the redox electrolyte in enhancing charge storage in AHZSIB.

2. Experimental

2.1. Preparation of Na-NiHCF

Na-NiHCF was prepared following a simple solution co-precipitation method reported elsewhere [6] but with small modifications. Briefly, a green solution was first prepared by dissolving $Ni(NO_3)_2{\cdot}H_2O$ (12 mmol) in 120 mL of distilled water. At that time, a yellow solution was also prepared by dissolving (6 mmol) sodium hexacyanoferrate ($Na_4[Fe(CN)_6]{\cdot}10H_2O$) in 280 mL of distilled water. Then, the green solution was added dropwise into the yellow solution under continuous stirring at room temperature (~25 °C). After one h of stirring, the mixed solution was kept at rest mode for 24 h to precipitate Na-NiHCF particles. The particles were then washed with distilled water and ethanol several times and collected using the centrifugation process. The collected Na-NiHCF particles were dried at 80 °C overnight, and the powder form of Na-NiHCF was ultimately obtained via grinding using a mortar.

2.2. Preparation of Na-NiHCF cathode electrode

To prepare the cathode electrode for AHZSIB, a cathodic slurry was first prepared by blending 80 wt% of Na-NiHCF (active material), 10 wt % of Super-P carbon (conductive additive), and 10 wt% of poly (vinylidene) fluoride (binder) with an N-methyl-2-pyrrolidone solvent. Then, the cathodic slurry was coated onto carbon felt (14φ mm) and dried at 80 °C in an oven for 12 h. The mass loading of active material (Na-NiHCF) on the carbon felt ranged from 3 to 3.5 mg/cm^2. The carbon felt was used after being pretreated in an oven at 500 °C for two h to obtain a hydrophilic surface [25].

2.3. Cell assembly

To assemble the AHZSIB, the Zn anode part was prepared first, similar to the coin cell. In brief, the NASICON (sodium (**NA**) **S**uper**I**onic **CON**ductor) ceramic separator ($Na_3Zr_2Si_2PO_{12}$) was fastened to the open and round top cap of the coin cell. Then, Zn was attached to a metal spacer and placed on the bottom lid with Na_2SO_4 (0.5 M)/$ZnSO_4$ (2 M) electrolyte. Finally, the top and bottom lids were combined and sealed to obtain a coin-type Zn anode part, as schematically illustrated in Fig. S1a. In the coin cell anode part, one side of the ceramic separator faced the Zn anode, and the other side faced the cathode electrode. Then, as schematically shown in Fig. S1b, AHZSIB was assembled by combining the anode coin cell part with the prepared Na-NiHCF cathode electrode. The cathodic compartment was filled with 0.1 mL of $Na_4[Fe(CN)_6]$ (0.1 M) or 0.1 mL of TEMPOL/Na_2SO_4 (0.1/0.5 M) as redox electrolytes. A 0.1 mL of Na_2SO_4 (1 M) was also employed as a reference electrolyte. AHZSIBs were assembled at room temperature (approximately 25 °C) in an ambient air atmosphere. The assembled AHZSIB was aged for 12 h before electrochemical testing to enhance the wettability of the Na-NiHCF cathode electrode with the respective electrolyte.

2.4. Electrochemical test

Cyclic voltammetry (CV) measurements of the redox electrolytes (TEMPOL/Na_2SO_4 and $Na_4[Fe(CN)_6]$) and Na-NiHCF in the Na_2SO_4 electrolyte and redox electrolytes (TEMPOL/Na_2SO_4 and Na-NiHCF, respectively) were performed at a scan rate of 10 mV/s using a three-electrode system with a glassy carbon electrode (GCE, 0.07 cm^2) as the working electrode, Ag/AgCl as the reference electrode, and Pt wire as the counter electrode. The CV of the redox electrolytes (TEMPOL/Na_2SO_4 and $Na_4[Fe(CN)_6]$) was performed using a Na-NiHCF uncoated GCE as the working electrode. For the CV measurements of Na-NiHCF in the Na_2SO_4 and redox electrolytes (TEMPOL/Na_2SO_4 and Na-NiHCF, respectively), a Na-NiHCF coated GCE was used as the working electrode (*preparation of the Na-NiHCF coated GCE is given in Supporting Information*). The CVs of the $Na_4[Fe(CN)_6]$ redox electrolyte and TEMPOL/Na_2SO_4 redox electrolyte were recorded between −0.2 and 0.65 V (vs. Ag/AgCl), and 0.4 and 0.75 V (vs. Ag/AgCl), respectively. The CVs of Na-NiHCF in the Na_2SO_4 electrolyte performed between 0 and 1 V (vs. Ag/AgCl) and those in redox electrolytes (TEMPOL/Na_2SO_4 and $Na_4[Fe(CN)_6]$) recorded between −0.2 and 1 V (vs. Ag/AgCl). The concentrations of the Na_2SO_4, TEMPOL/Na_2SO_4, and $Na_4[Fe(CN)_6]$ electrolytes were 1 M, 0.1 M/0.5 M, and 0.1 M, respectively.

CV measurements in the $Na_2SO_4/ZnSO_4$ electrolyte and $ZnSO_4$ electrolyte were also performed to study the redox reaction of the Zn^{2+}/Zn pair at a scan rate of 10 mV/s using Ti foil (~1 cm^2) as the working electrode, Ag/AgCl as the reference electrode, and Zn as the counter electrode. The concentrations of the $Na_2SO_4/ZnSO_4$ and $ZnSO_4$ electrolytes were 0.5 M/2 M and 2 M, respectively.

The Galvanostatic charge-discharge (GCD) performance of the above assembled AHZSIBs was recorded at various current densities (from 0.15 to 1.5 mA/cm^2) based on the area of the electrode. For the comparative

GCD cycle performance study, AHZSIB with the Na_2SO_4 (1 M), TEMPOL/Na_2SO_4 (0.1 M/0.5 M), and $Na_4[Fe(CN)_6]$ (0.1 M) electrolytes were tested at 0.15 mA/cm^2, separately. The prolonged GCD cycle performance of AHZSIB with the $Na_4[Fe(CN)_6]$ electrolyte was tested at 1.25 mA/cm^2. In this study, all the provided specific capacity and energy density value were calculated with respect to the mass of the Na-NiHCF cathode active material.

CV investigations were performed using an SP150 Biologic multichannel electrochemical workstation. GCD studies of the AHZSIB were performed using a Wonatech (WBCS 3000) electrochemical workstation. All the electrochemical characterizations were performed at room temperature (approximately 25 °C).

3. Results and discussion

Fig. 1a and b show the schematic AHZSIB structure and the possible electrochemical reactions that occur at the anode and cathode during the charge/discharge process for a conventional AHZSIB and a redox electrolyte-based AHZSIB, respectively. The conventional AHZSIB consisted of a Zn anode and a Na^+ ion insertion/deinsertion cathode embedded with a mixed Na^+/Zn^{2+} ion-based electrolyte and separated by ion-permeable separators (e.g., cellulose and glass fiber). The redox electrolyte-based AHZSIB consisted of a Zn anode that was immersed in a mixed Na^+/Zn^{2+} ion-based electrolyte and a Na^+ ion insertion/deinsertion cathode that was immersed in a Na^+ ion-based redox-active electrolyte and separated by a $Na_3Zr_2Si_2PO_{12}$ ceramic separator. The $Na_3Zr_2Si_2PO_{12}$ separator is an ion-selective membrane that only permits the transport of Na^+ between the anode and cathode, thereby avoiding

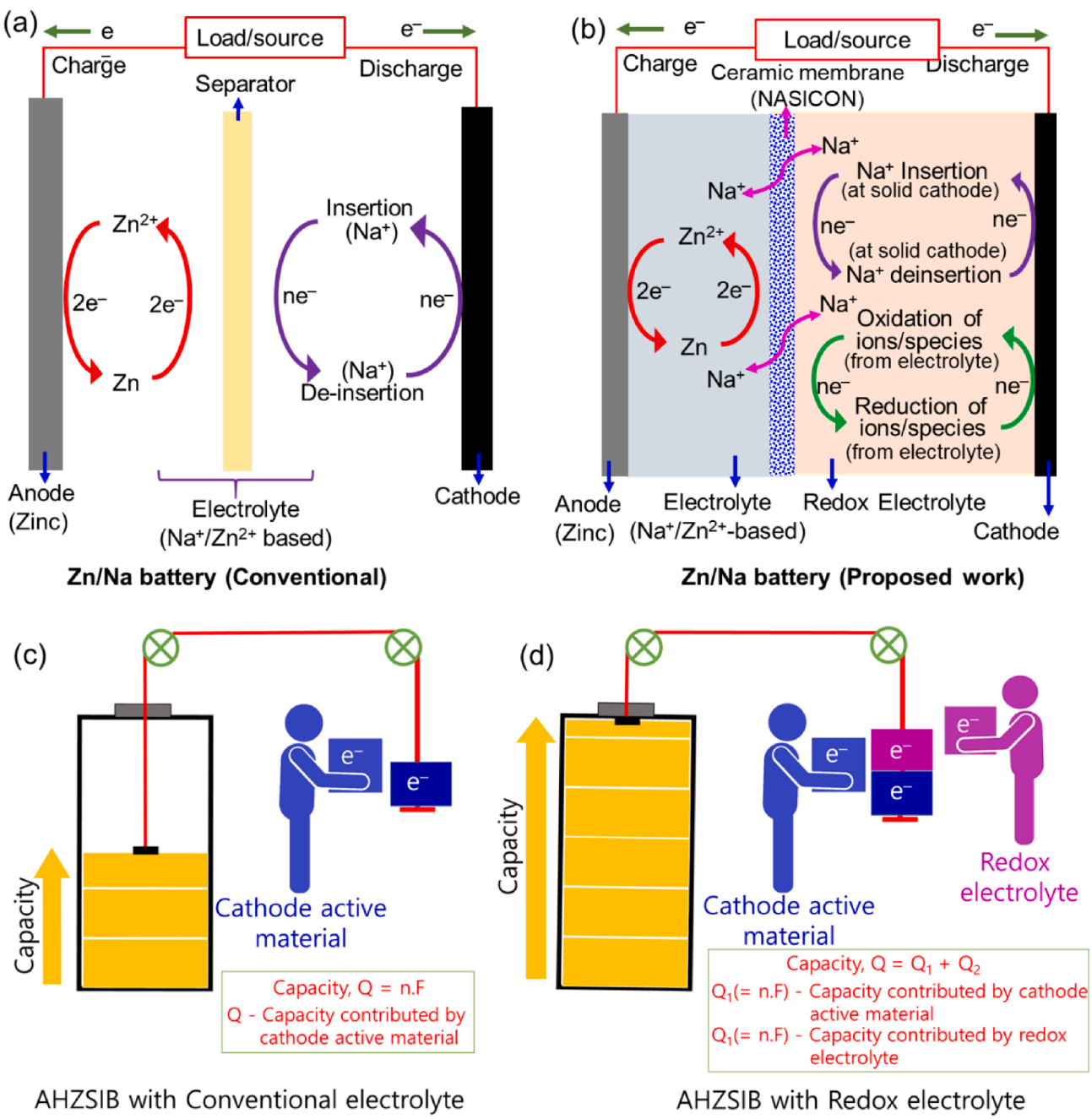

Fig. 1. Schematic cell structure of a conventional AHZSIB (a) and redox electrolyte-based AHZSIB (b). Schematic diagram that represents the capacity storage ability of AHZSIB using the conventional electrolyte (c) and redox electrolyte (d).

the shuttle effect associated with the contamination of the anodic part with a redox electrolyte present in the cathode. In a conventional AHZSIB, as shown in Fig. 1a, the Zn deposition/dissolution process occurs at the anode, and Na^+ ion deinsertion/insertion occurs at the cathode during the charge/discharge process. Thus, owing to the ensuing single electrochemical redox reaction, Faraday's law for the capacity (i.e., the amount of charge) at the cathode side of a conventional AHZSIB can be simply expressed as Q = n.F, where n is the number of electrons (e^-), and F is the Faraday constant. In the redox electrolyte-based AHZSIB, a similar Zn deposition/dissolution process occurs at the anode. However, the apparent differences are shown at the cathode side (Fig. 1b), where along with the Na^+ ion deinsertion/insertion process (purple arrows in Fig. 1b), highly soluble redox species from the electrolyte can also undergo a reversible redox (oxidation/reduction) reaction at the cathode (green arrows in Fig. 1b). Based on the occurrences of these two different electrochemical redox processes in the proposed redox electrolyte-based AHZSIB, the total amount of electron (e^-) generation at the cathode side can increase. Therefore, the Faraday's law for the capacity at the cathode side of the redox electrolyte-based AHZSIB can be expressed as $Q = Q_1 + Q_2$, where Q_1 (=n.F) denotes the capacity contributed by Na^+ ion deinsertion/insertion cathode active material and Q_2 (=n.F) represents the capacity contributed by the redox electrolyte. Fig. 1c and d illustrate the capacity storage abilities of the conventional and redox electrolytes, respectively. The conventional electrolyte-based AHZSIB has a limited charge storage capacity owing to the lone capacity contribution of the cathode. The redox electrolyte-based AHZSIB has an enhanced charge storage capacity because of the combined capacity contribution of the cathode and redox electrolyte.

Several choices of Na^+ ion deinsertion/insertion materials for cathodes (e.g., $Na_{0.44}MnO_2$, $Na_2NiFe(CN)_6$ and $Na_3V_2(PO_4)_3$) [6–10] and redox molecules/compounds (e.g., $Na_4[Fe(CN)_6]$, TEMPOL and hydroquinone) [21,26–31] for the preparation of the aqueous redox electrolyte are available to develop the AHZSIB proposed above (Fig. 1C). In this study, to demonstrate proof-of-concept, we chose sodium nickel hexacyanoferrate ($Na_2NiFe(CN)_6$, (Na-NiHCF)) as the cathode material because of its excellent electrochemical cycle stability, chemical stability in an aqueous electrolyte (7–8.5 pH), and easy synthesis [6,32–34]. Two types of redox-active compounds, i.e., TEMPOL and $Na_4[Fe(CN)_6]$, were selected to prepare the redox electrolytes because both are commercially available, water-soluble, and can offer highly reversible redox features at a positive potential. Accordingly, TEMPOL and $Na_4[Fe(CN)_6]$ are well-known redox electrolyte compounds in redox flow batteries [26,29,35,36]. TEMPOL is an organic compound, and $Na_4[Fe(CN)_6]$ is a metalorganic compound, and both can be used in the near-natural pH electrolyte [22,29], which is chemically compatible with the Na-NiHCF cathode. However, it was necessary to add Na^+ cations containing salts such as NaCl or Na_2SO_4 in TEMPOL redox electrolyte to obtain sufficient ionic conductivity and sufficient free Na^+ ions to be inserted/deinserted into/from Na-NiHCF during cycling. Therefore, in this study, the Na_2SO_4 dissolved TEMPOL redox electrolyte was used in the AHZSIB (*hereafter referred to as the TEMPOL/Na_2SO_4 redox electrolyte*). Nevertheless, the $Na_4[Fe(CN)_6]$ – based redox electrolyte can be prepared without any addition of Na^+ cations containing salt because this compound is a salt that can supply sufficient free Na^+ ions to be inserted/deinserted into/from Na-NiHCF.

In this study, a Na-NiHCF cathode material was synthesized via a simple precipitation method (*for details, see the Experimental section*). The

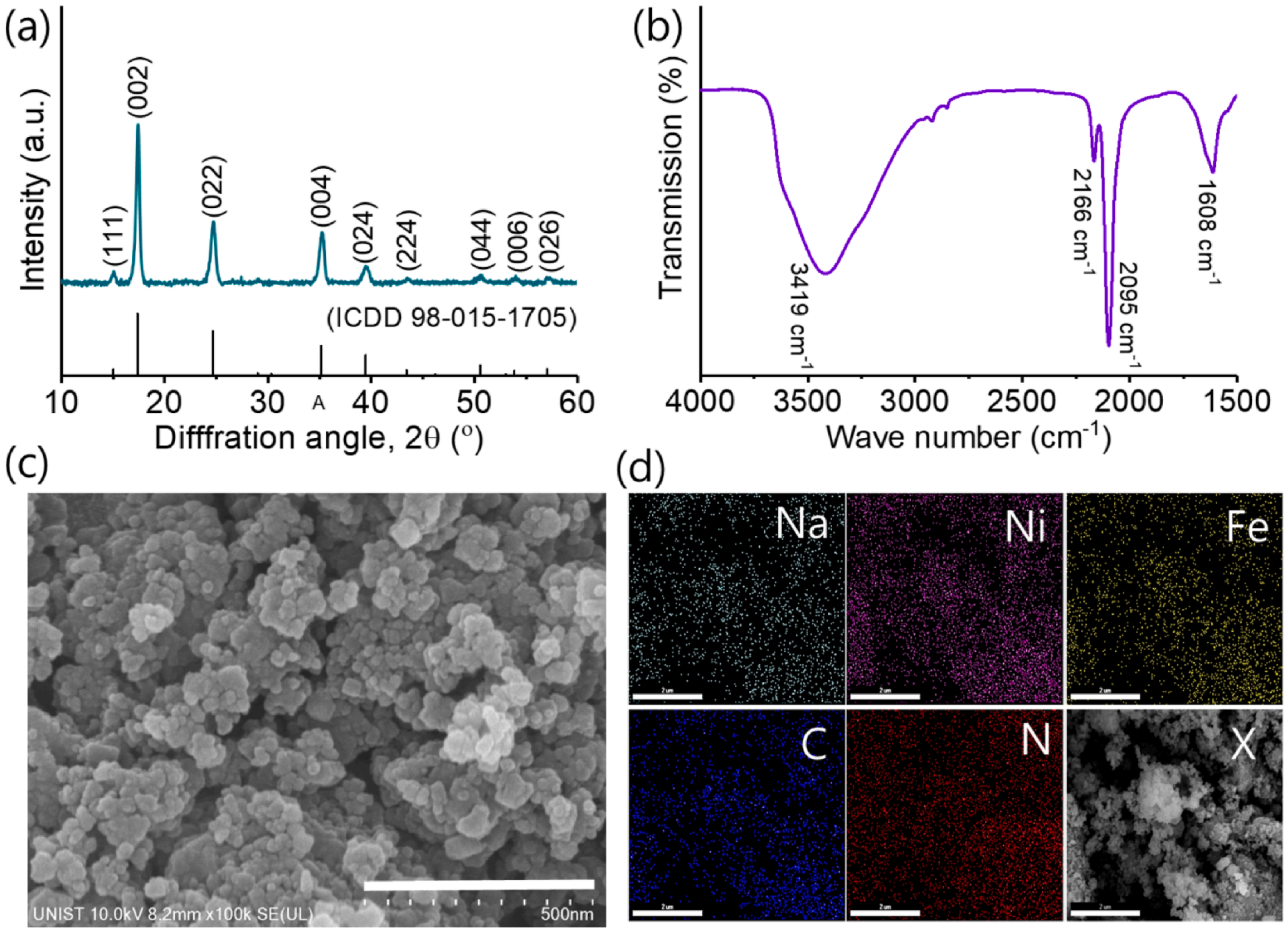

Fig. 2. XRD pattern (a), FT-IR spectra (b), SEM image (c), and EDAX images (d) of as-prepared SNHCF. In (d), X is the SEM image of SNHCF that was used for EDAX mapping. The scale bar for the SEM image (c) is 500 nm and that for the EDAX images (d) is 2 μm.

XRD pattern of the as-prepared Na-NiHCF is shown in Fig. 2a. All the observed peaks (2θ) and the plane (hlk) values shown in Fig. 2a indicate that the as-prepared Na-NiHCF is a Prussian blue crystalline structure (ICDD No. 98–015-1705) with a face-centered cubic phase. The sharp and well-split peaks indicate the high degree of crystallinity of the as-prepared Na-NiHCF. In addition, no impurity peaks were observed in the XRD pattern of Na-NiHCF. In the FTIR spectra (Fig. 2b), the detected peaks at 2095 cm^{-1} and 2166 cm^{-1} corresponded to the stretching vibration of the C≡N legends, which coordinated to Fe^{2+} and Ni^{2+} (i.e., Fe^{2+}–C≡N–Ni^{2+}) and Fe^{3+} and Ni^{2+} (i.e., Fe^{3+}–C≡N–Ni^{2+}), respectively [37]. This result corroborates the formation of the metalorganic framework in the as-prepared Na-NiHCF. The resultant peak of Fe^{3+}–C≡N–Ni^{2+} arises from the oxidation of Fe^{2+} in Fe^{2+}–C≡N–Ni^{2+}, which typically occurs during the preparation of Na-NiHCF. The peaks at 3419 and 1608 cm^{-1} are related to the hydroxyl group (O–H) stretching and bending mode of water (H_2O), which generally originates from the lattice water in the as-prepared Na-NiHCF [6,38]. The SEM image (Fig. 2c) shows that the as-prepared Na-NiHCF powder is composed of agglomerated nanoparticles with a size of 10–20 nm and an irregular shape. The EDAX images (Fig. 2d) and spectra (Fig. S2) verify the presence of Na, Ni, Fe, C, and N in the as-prepared Na-NiHCF.

$$Fe^{2+}(CN)_6^{4-} \underset{\text{Discharge}}{\overset{\text{Charge}}{\rightleftharpoons}} Fe^{3+}(CN)_6^{3-} + e^- \quad (1)$$

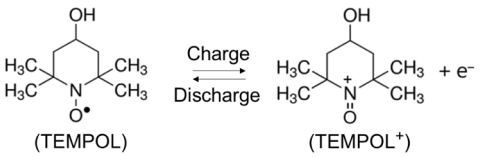

(2)

$$Na_xNiFe^{2+}(CN)_6 \underset{\text{Discharge}}{\overset{\text{Charge}}{\rightleftharpoons}} Na_{x-y}NiFe^{3+}(CN)_6 + yNa^+ + ye^- \quad (3)$$

First, the electrochemical features of $Na_4[Fe(CN)_6]$ and TEMPOL/Na_2SO_4 redox electrolytes were individually studied via CV in three-electrode electrochemical cells. As displayed in Fig. 3a, both redox electrolytes show their corresponding redox states. The redox peak observed for the $Na_4[Fe(CN)_6]$ redox electrolyte was correlated to the $Fe^{2+}(CN)_6^{4-}/Fe^{3+}(CN)_6^{3-}$ (i.e., ferrocyanide/ferricyanide) redox pair (see Eq. (1)) [26,39]. The redox peak for the TEMPOL/Na_2SO_4 redox electrolyte corresponded to the redox pair TEMPOL/$TEMPOL^+$ (see Eq. (2)) [29,40]. The obtained redox potential for the $Fe^{2+}(CN)_6^{4-}/Fe^{3+}(CN)_6^{3-}$ redox pair was 0.2 V (vs. Ag/AgCl), and that for the TEMPOL/$TEMPOL^+$ redox pair was 0.63 V (vs. Ag/AgCl) (Fig. 3a). Notably, the redox potential of the TEMPOL/$TEMPOL^+$ redox pair was ~0.33 V is higher than that of the $Fe^{2+}(CN)_6^{4-}/Fe^{3+}(CN)_6^{3-}$ redox pair.

The electrochemical characteristics of the Na-NiHCF cathode material were also studied via CV in a three-electrode electrochemical cell using the $Na_4[Fe(CN)_6]$ and TEMPOL/Na_2SO_4 based redox electrolytes and the Na_2SO_4 electrolyte as a separate reference. Na-NiHCF in the Na_2SO_4 electrolyte showed a reversible redox peak at a potential of 0.53 V (Fig. 3b and c). This observed redox peak (0.53 V vs. Ag/AgCl) corresponded to the redox reaction of Fe^{2+}/Fe^{3+} that occurred in the lattice of Na-NiHCF. Moreover, during this Fe^{2+}/Fe^{3+} redox reaction at Na-NiHCF, the Na^+ ions' deinsertion/insertion processes also spontaneously occur with Na-NiHCF to maintain crystalline charge neutrality (Eq. (3)) [32,38,41]. The CV curve of the Na-NiHCF in $Na_4[Fe(CN)_6]$ redox electrolyte displays a single redox peak with an enhanced current area compared to the CV of Na-NiHCF in Na_2SO_4 electrolyte (Fig. 3b). The enhanced current area reveals the occurrence of the combined redox reaction (i.e., Eqs. (1) and (3)) of the $Fe^{2+}(CN)_6^{4-}/Fe^{3+}(CN)_6^{3-}$ redox pair from the electrolyte and Fe^{2+}/Fe^{3+} redox pair in the lattice of Na-NiHCF. The observed single redox peak, even though two different redox reactions occurred, may have resulted from the complete overlap of two redox peaks associated to the reaction of $Fe^{2+}(CN)_6^{4-}/Fe^{3+}(CN)_6^{3-}$ from the electrolyte and Fe^{2+}/Fe^{3+} at Na-NiHCF lattice [22,23]. Similarly, the Na-NiHCF in the TEMPOL/Na_2SO_4 redox electrolyte also displayed an

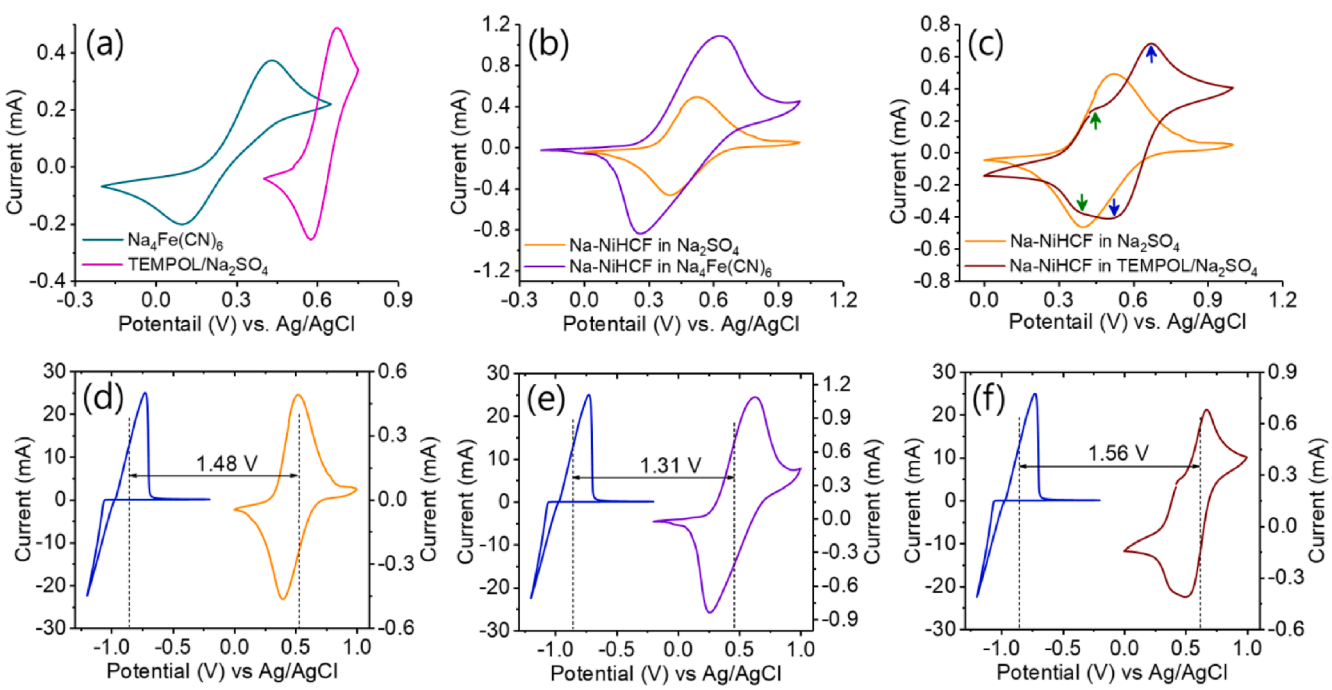

Fig. 3. (a) Comparision of CV curves of the TEMPOL/Na_2SO_4 (0.1/0.5 M) and $Na_4[Fe(CN)_6]$ redox electrolytes. (b) CV curve of Na-NiHCF in the $Na_4[Fe(CN)_6]$ (0.1 M) redox electrolyte and a comparison with the Na_2SO_4 (1 M) electrolyte. (c) CV curve of Na-NiHCF in TEMPOL/Na_2SO_4 (0.1/0.5 M) redox electrolyte and a comparison with the Na_2SO_4 (1 M) electrolyte. Combined CV curves of (d) Zn in the measured $ZnSO_4/Na_2SO_4$ (2 M/0.5 M) electrolyte and Na-NiHCF measured in the Na_2SO_4 (1 M) electrolyte. (e) Zn measured in the $ZnSO_4/Na_2SO_4$ (2 M/0.5 M) electrolyte and Na-NiHCF measured in the $Na_4[Fe(CN)_6]$ (0.1 M) redox electrolyte. (f) Zn measured in the $ZnSO_4/Na_2SO_4$ (2 M/0.5 M) electrolyte and Na-NiHCF measured in TEMPOL/Na_2SO_4 (0.1/0.5 M) redox electrolyte. Here, all the CV curves are recorded at 10 mV/s.

improved current area in the obtained CV curve (Fig. 3c) owing to the combined redox reaction (i.e., Eqs. (2) and (3)) of the TEMPOL/TEMPOL$^+$ redox pair from the electrolyte and Fe^{2+}/Fe^{3+} redox pair in the lattice of Na-NiHCF. In addition, two redox peaks were observed in the CV (see the indicated arrows in Fig. 3c), corresponded to the redox reaction of TEMPOL/TEMPOL$^+$ from the electrolyte (green arrow) and $Fe^{2+/}Fe^{3+}$ at Na-NiHCF lattice (blue arrow). However, these increased current characteristics implied an enhancement of the overall charge capacity. A similar tendency, i.e., an overall charge storage capacity enhancement can be expected when combing the redox electrolyte (i.e., $Na_4[Fe(CN)_6]$ or TEMPOL/Na_2SO_4) and Na-NiHCF in the AHZSIB.

The CV shown in Fig. S3 indicates that the presence of hybrid ions (Na^+/Zn^{2+}) in the electrolyte did not modify the electrochemical properties of the Zn^{2+}/Zn reaction (i.e., $Zn^{2+} + 2e^- \leftrightarrow Zn$) at the Zn anode. Moreover, based on the CV curves of the cathodic and anodic semi reactions, we can expect a discharge cell voltage of 1.48 V for the Na_2SO_4 electrolyte (Fig. 3d), 1.31 V for the $Na_4[Fe(CN)_6]$ redox electrolyte (Fig. 3e), and 1.56 V for the TEMPOL/Na_2SO_4 redox electrolyte (Fig. 3f).

As shown in Fig. S1, AHZSIBs were assembled using a TEMPOL/Na_2SO_4 redox electrolyte and $Na_4[Fe(CN)_6]$) redox electrolyte in contact with Na-NiHCF at the cathode side, which was separated from the anode side ($ZnSO_4/Na_2SO_4$ mixed electrolyte and Zn foil) by a Na^+ ion-selective $Na_3Zr_2Si_2PO_{12}$ ceramic membrane. For comparative studies, AHZSIBs were also assembled using a conventional (non-redox) Na_2SO_4 electrolyte. Then, the assembled AHZSIBs were subjected to galvanostatic charge/discharge to determine the influences of electrolytes (i.e., Na_2SO_4, TEMPOL/Na_2SO_4, and $Na_4[Fe(CN)_6]$) on battery performance, especially the capacity and cycle stability performance. Fig. 4a shows the first charge/discharge curve for the three different electrolytes using AHZSIB at 0.15 mA/cm^2 between 0.8 and 1.9 V (vs. Zn^{2+}/Zn). These results show that when introducing the redox electrolyte at the cathode side, the storage capacity of AHZSIB increased remarkably. Specifically, the discharge capacity of AHZSIB with the Na_2SO_4 electrolyte was only 49 mAh/g, but it was boosted to 120 mAh/g with the TEMPOL/Na_2SO_4 redox electrolyte and to 144 mAh/g with the $Na_4[Fe(CN)_6]$ redox electrolyte (Fig. 4a and b, respectively). The low capacity (i.e., 49 mAh/g) from the Na_2SO_4 electrolyte indicates the sole capacity contribution of Na-NiHCF cathode (Fig. 4b). The capacity increase from 49 mAh/g to 144 mAh/g (or 120 mAh/g) after using redox electrolytes designated the combined capacity contribution of the Na-NiHCF cathode and redox species ($Fe^{2+}(CN)_6^{4-}/Fe^{3+}(CN)_6^{3-}$ or TEMPOL/TEMPOL$^+$) dissolved in the redox electrolyte (Fig. 4b). This corroborates our initial expectation for the above CV results.

At the first cycle, AHZSIB tested with the Na_2SO_4 electrolyte and $Na_4[Fe(CN)_6]$ redox electrolyte (Fig. 4a), respectively, resulted in a higher discharge capacity than the charge capacity (i.e., a >100% coulombic efficiency). This may have resulted from the low Na^+ content in the as-prepared Na-NiHCF, and this kind of behavior is typical for Prussian blue-based materials [5,8,42,43]. However, for both cases, the discharge capacity remained close to the charge capacity (i.e., ~100% coulombic efficiency) from the second cycle onward (Fig. 4c and S4). In contrast, AHZSIB with the TEMPOL/Na_2SO_4 redox electrolyte exhibited a lower discharge capacity than the charge capacity (i.e., <100 of coulombic efficiency) in the first cycle (Fig. 4a and Fig. S4). This may be attributed to the irreversibility of the oxidized TEMPOL$^+$ species caused by their chemical side reactions [40]. The attained discharge cell voltages for Na_2SO_4, $Na_4[Fe(CN)_6]$ and TEMPOL/Na_2SO_4 electrolytes were 1.31 V (vs. Zn^{2+}/Zn), 1.22 V(vs. Zn^{2+}/Zn), and 1.38 V (vs. Zn^{2+}/Zn), respectively. The tested AHZSIB with the $Na_4[Fe(CN)_6]$ redox

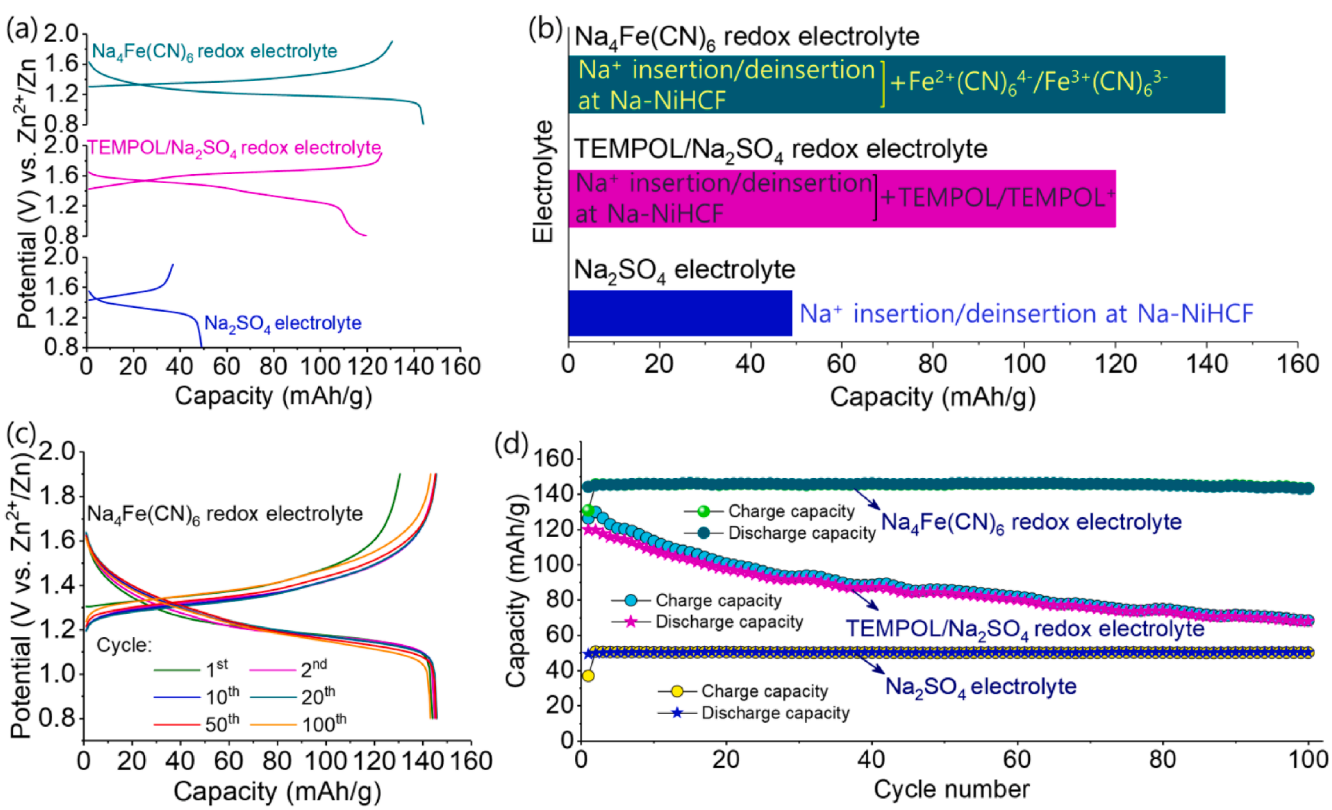

Fig. 4. (a) First charge and discharge curve of the TEMPOL/Na_2SO_4 (0.1 M/0.5 M) electrolyte-based AHZSIB and the $Na_4[Fe(CN)_6]$ electrolyte-based AHZSIB and their comparison with the Na_2SO_4 (1 M) electrolyte-based AHZSIB (at 0.15 mA/cm^2). (b) A graph to showing the capacity contributions of the Na_2SO_4 electrolyte and redox electrolytes (TEMPOL/Na_2SO_4 and $Na_4[Fe(CN)_6]$). (c) 1st, 2nd, 10th, 20th, 50th and 100th charge–discharge curves of the $Na_4[Fe(CN)_6]$ (0.1 M) electrolyte-basedAHZSIB (at 0.15 mA/cm^2). (d) Cycling performance of the TEMPOL/Na_2SO_4 (0.1 M/0.5 M) electrolyte-based AHZSIB and $Na_4[Fe(CN)_6]$ (0.1 M) electrolyte-based AHZSIB and their comparison with the Na_2SO_4 (1 M) electrolyte-based AHZSIB (at 0.15 mA/cm^2). The capacity is normalized based on the mass of the Na-NiHCF cathode material. All the charge and discharge tests were performed between 0.8 and 1.9 V (vs. Zn^{2+}/Zn).

electrolyte exhibited a higher energy density (175 Wh/kg) than AHZSIB that tested with the TEMPOL/Na_2SO_4 redox electrolyte (165 Wh/kg) and Na_2SO_4 electrolyte (64 Wh/kg).

After 100 repeated charge and discharge cycles at 0.15 mA/cm^2 between 0.8 and 1.9 V (vs. Zn^{2+}/Zn), the capacity was 143 mAh/g for the $Na_4[Fe(CN)_6]$ redox electrolyte, 50 mAh/g for the Na_2SO_4 electrolyte, and 68 mAh/g for the TEMPOL/Na_2SO_4 redox electrolyte. These values represented a capacity retention close to 100% for Na_2SO_4 and $Na_4[Fe(CN)_6]$ electrolytes, but only 50% for the TEMPOL/Na_2SO_4 electrolytes (Fig. 4d). For the TEMPOL/Na_2SO_4 electrolyte, the voltage profile rapidly changed, and the discharge capacity decreased with increasing cycles (Fig. S5a). The capacity part contributed by the TEMPOL/TEMPOL$^+$ redox pair decreased prominently, as shown in Fig. S5a. This may have resulted from the poor electrochemical stability of the TEMPOL/TEMPOL$^+$ redox pair. The electrochemical stability of TEMPOL could be attributed to the presence of O_2 in the electrolyte or its undesirable side reactions such as irreversible ring cleavage under oxidation [40,44,45]. Interestingly, for the Na_2SO_4 electrolyte and $Na_4[Fe(CN)_6]$ redox electrolyte (Fig. S5b and Fig. 4c, respectively), there were no predominant changes in the voltage profiles, and no capacity fading was observed throughout 100 successive repeated cycles. This suggests the excellent electrochemical stability of Na-NiHCF and the combination of Na-NiHCF and $Fe^{2+}(CN)_6^{4-}/Fe^{3+}(CN)_6^{3-}$ redox pairs.

The rate performance of the $Na_4[Fe(CN)_6]$ redox electrolyte-based AHZSIB was scrutinized at different current densities from 0.15 to 1.5 mA/cm^2, and the corresponding results are shown in Fig. 5a and b. Using this battery, the capacities of 144, 143, 140, 137, 133, 130, 124, 111 and 78 mAh/g were delivered at 0.15, 0.2, 0.3, 0.4, 0.6, 0.8, 1, 1.25 and 1.5 mA/cm^2, respectively. Fig. 5b shows that the capacity and cell voltage decreased with increasing current density. The decrease in the cell voltage was mainly caused by the increase in the overall resistance with the current density. Notably, the obtained capacity (i.e., 78 mAh/g) at 1.5 mA/cm^2 was 53% of the capacity at 0.15 mA/cm^2. The decrease in the capacity at high current density might have been caused by the slow redox kinetics of the $Fe^{2+}(CN)_6^{4-}/Fe^{3+}(CN)_6^{3-}$ redox species dissolved in the electrolyte and the poor utilization of Na^+ insertion/deinsertion at the Na-NiHCF cathode. Na^+ ion insertion/deinsertion at the solid materials is an extremely slow process (diffusion-limited) compared to the redox reaction of the redox pair dissolved in the electrolyte. Therefore, the large capacity decrease at the high current density could mainly be attributed to Na^+ ion insertion/deinsertion at the Na-NiHCF cathode. The rate performance test of the AHZSIB using the Na_2SO_4 electrolyte (in the absence of redox species) confirms this expectation since only 4% of the capacity (i.e., 2 mAh/g) attributed to Na^+ insertion/deinsertion was maintained at 1.5 mA/cm^2 (Fig. S6). Based on this result, it estimated that in the obtained capacity of 78 mAh/g at 1.5 mA/cm^2 (Fig. 5a and 5b), ~76 mAh/g of capacity contributing by $Fe^{2+}(CN)_6^{4-}/Fe^{3+}(CN)_6^{3-}$ redox pairs and only ~2 mAh/g of capacity contributing by the Na-NiHCF cathode through Na^+ ion insertion/deinsertion process.

Fig. 5b shows that 100% of the capacity was retrieved returning from 1.5 mA/cm^2 to 0.15 mA/cm^2, which indicated a quick capacity recoverability of the $Fe^{2+}(CN)_6^{4-}/Fe^{3+}(CN)_6^{3-}$ redox species and the Na-NiHCF cathode in the AHZSIB. Overall, Fig. 5b reveals that the $Na_4[Fe(CN)_6]$ redox electrolyte simultaneously enhanced the specific capacity and energy and improved the rate capability of AHZSIB. The excellent long-term cycling ability of the $Na_4[Fe(CN)_6]$ redox electrolyte-based AHZSIB at a high current density of 1.25 mA/cm^2 is shown in Fig. 5c. Thereby, the capacities of 104 and 110 mAh/g were attained at the first and 500th cycles, respectively. This indicated that the obtained discharge capacity at the first cycle closer to the discharge capacity gained at the 500th cycle. The observed capacity decreases and increases during the cycles (Fig. 5c) may have been caused by the formation of hydrogen bubbles on the surface of the Zn anode and diffusion of hydrogen bubbles from the surface of the Zn anode, respectively [46]. In brief, the Zn^{2+}/Zn redox reaction occurs near the hydrogen evolution potential; therefore, during the charging process, hydrogen bubbles can form on the surface of the Zn anode. Therefore, these formed hydrogen bubble sizes can increase by increasing the cycle number, and the formed bubbles take time (a few

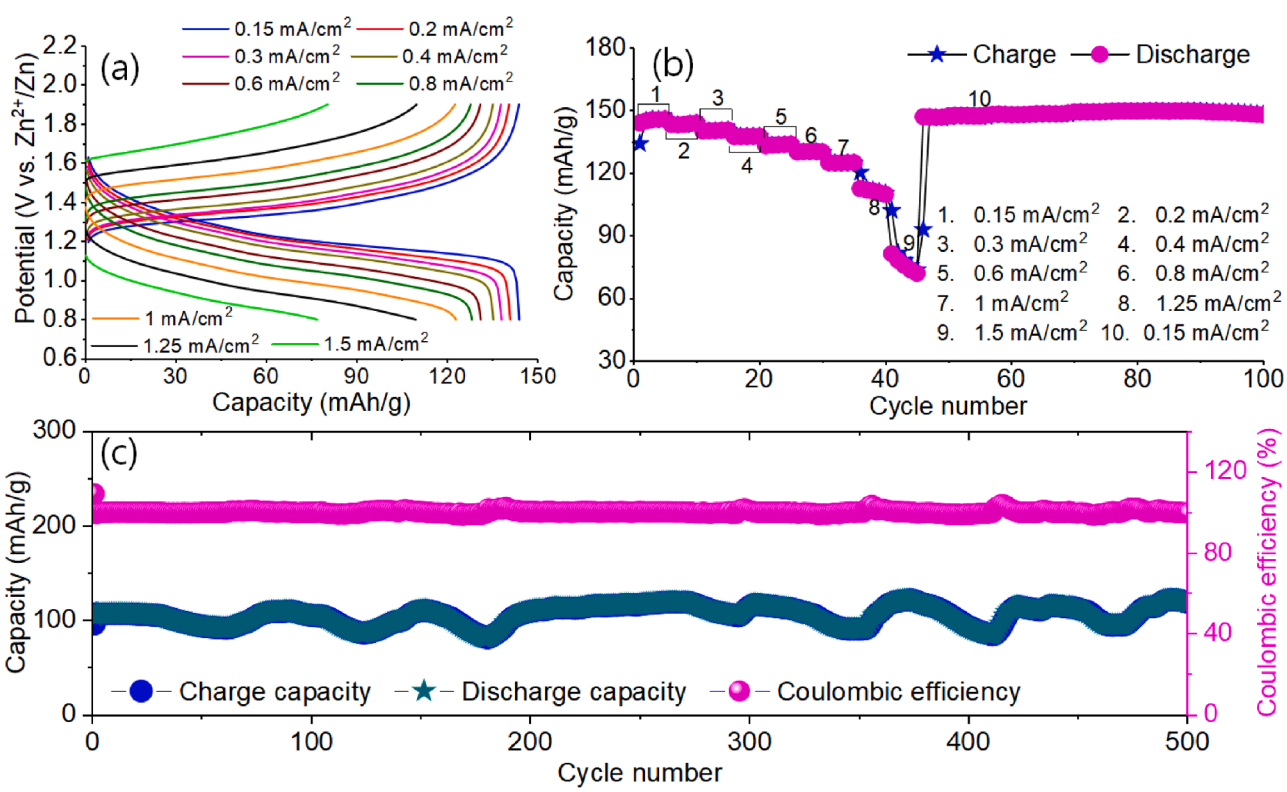

Fig. 5. (a) Charge-discharge curves at different current densities from 0.15 to 1.5 mA/cm^2. (b) Rate performances, and (c) Cycle stability (at 1.25 mA/cm^2) of AHZSIB tested with the $Na_4[Fe(CN)_6]$ (0.1 M) electrolyte.

cycles) to diffuse from the surface of the Zn anode. In the meantime, the formed hydrogen bubble can reduce the active area on the Zn anode for the Zn^{2+}/Zn redox reaction, causing a capacity decrease with cycling. After the hydrogen bubbles began diffusing away from the surface of the Zn anode, the active area for the Zn/Zn^{2+} redox reaction be increased, thus increased the capacity with the cycles [46]. However, we can conclude that the observed cycle performance at 1.25 mA/cm^2 confirms the excellent electrochemical stability of both the $Fe^{2+}(CN)_6^{4-}$/$Fe^{3+}(CN)_6^{3-}$ redox pair and Na-NiHCF cathode.

Even though redox electrolytes can enhance the capacity storage of AHZSIB, there are still some practical challenges remaining, including a low current operation, low cell voltage, low capacity, complication in cell assembly; these demands require further research. The current challenges and their mitigation strategies to build an advanced high-performance redox electrolyte AHZSIB (Fig. 6) are briefly addressed as follows: **(i). *Low current/power density:*** The devised AHZSIB operated at low current densities (in mA/cm^2) (Fig. 4a) due to the high ionic resistance of the $Na_3Zr_2Si_2PO_{12}$ ceramic separator, which resulted in a low power performance (see Fig. S7). However, the power performance can be improved by replacing the $Na_3Zr_2Si_2PO_{12}$ separator with highly ionic conductive polymer-based membranes, such as Nafion membranes (Fig. 6). $Na_3Zr_2Si_2PO_{12}$ was used in this study to demonstrate the proof-of-concept study of redox electrolyte-based AHZSIB. **(ii). *Low cell voltage:*** The cell voltage obtained in this work for AHZSIB was <1.4 V, which is still a limitation in achieving high energy density. However, the practical cell voltage of AHZSIB can be further improved using two methods (Fig. 6). One is using alkaline electrolyte with a Zn anode, which can help to raise the cell voltage to 1.8 V. This is because the redox potential of the Zn/$[Zn(OH)_4]^{2-}$ pair (−1.25 V vs. SHE) generated in alkaline electrolytes is lower than that of the redox potential of Zn/Zn^{2+} pair (−0.76 V vs. SHE) that is generated in near-neutral (or acidic) electrolytes [47,48]. The second method is pairing a high-voltage cathode with a Zn anode. A pair of Zn and $Na_2Zn_3[Fe(CN)_6]_2$ can potentially deliver a cell voltage of 1.8 V [49] and Zn and $Na_2MnFe(CN)_6$(+) may offer a cell voltage of 2 V [50]. **(iii). Low Capacity:** Similar to the cell voltage, a high capacity is also essential to reach a high energy density. The capacity at the cathode side in AHZSIB can be further increased by combining a high-capacity cathode (e.g., $Na_3V_2(PO_4)_3$ and $Na_2MnFe(CN)_6$) [13,50] and a highly concentrated $Na_4[Fe(CN)_6]$ redox electrolyte (~0.6 M) or any other highly concentrated redox electrolyte (e.g., functionalized ferrocene-based redox electrolyte) (Fig. 6) [28]. However, when using a highly concentrated redox electrolyte, some other issues such as ionic conductivity, viscosity, reversibility of redox pair and utilization of redox pair might be penalized so it will be necessary to optimize the concentration of the redox electrolyte to get a good trade-off. In this context, the redox pair in the redox electrolyte, which can supply more than one electron during the redox reaction, may have the most potential (e. g., Br_2/Br^-, I_3^-/I^-, and hydroquinone/quinone) [18,21,51] to enhance the capacity of AHZSIB while keeping low concentrations (Fig. 6). **(iv). *Complexity in cell assembly:*** The use of the $Na_3Zr_2Si_2PO_{12}$ membrane in AHZSIB creates complications during battery cell assembly. This complication can be simplified using a gelled electrolyte-covered Zn anode (Fig. 6), as reported elsewhere for Zn-MnO_2 batteries [52]. Notably, the implementation of a gel electrolyte for Zn anodes could be a potential replacement for the expensive ion-exchange membrane; therefore, we can expect an improved power performance.

4. Conclusion

In this work, to promote the capacity storage of hybrid Zn^{2+}/Na^+ ion batteries (AHZSIB), we have integrated redox electrolytes based on $Na_4[Fe(CN)_6]$ or TEMPOL/Na_2SO_4 with Na^+ deinsertion/insertion sodium nickel hexacyanoferrate (Na-NiHCF) cathode. Interestingly, compared to the conventional (non-redox) Na_2SO_4 electrolyte, the tested redox electrolytes in the AHZSIB enhanced the overall capacity by more than two-fold. The achieved capacity for AHZSIB with the TEMPOL/Na_2SO_4 redox electrolyte was 120 mAh/g, and that with $Na_4[Fe(CN)_6]$ redox electrolyte was 144 mAh/g; however, that with Na_2SO_4 electrolyte was only 49 mAh/g. Despite this result, AHZSIB with the TEMPOL/Na_2SO_4 redox electrolyte showed poor cycle stability compared to that of the $Na_4[Fe(CN)_6]$ redox electrolyte. At 0.15 mA/cm^2, nearly 100% of the discharge capacity retention was obtained for the AHZSIB with the $Na_4[Fe(CN)_6]$ redox electrolyte, but this value was only 50% for AHZSIB with the TEMPOL/Na_2SO_4 redox electrolyte. Even at a high current density of 1.25 mA/cm^2, the AHZSIB with the $Na_4[Fe(CN)_6]$ redox electrolyte maintained 100% of the discharge capacity retention for over 500 cycles. This study validates the ability of the redox electrolyte to boost the capacity storage of AHZSIB. We foresee that the use of electrolytes with redox characteristics will become an important step toward developing high energy density stationary AHZSIBs used to ensure adequate energy storage applications. However, as specified in the discussion section, further future research and development (R&D) is required to construct an effective and scalable redox electrolyte-based AHZSIB.

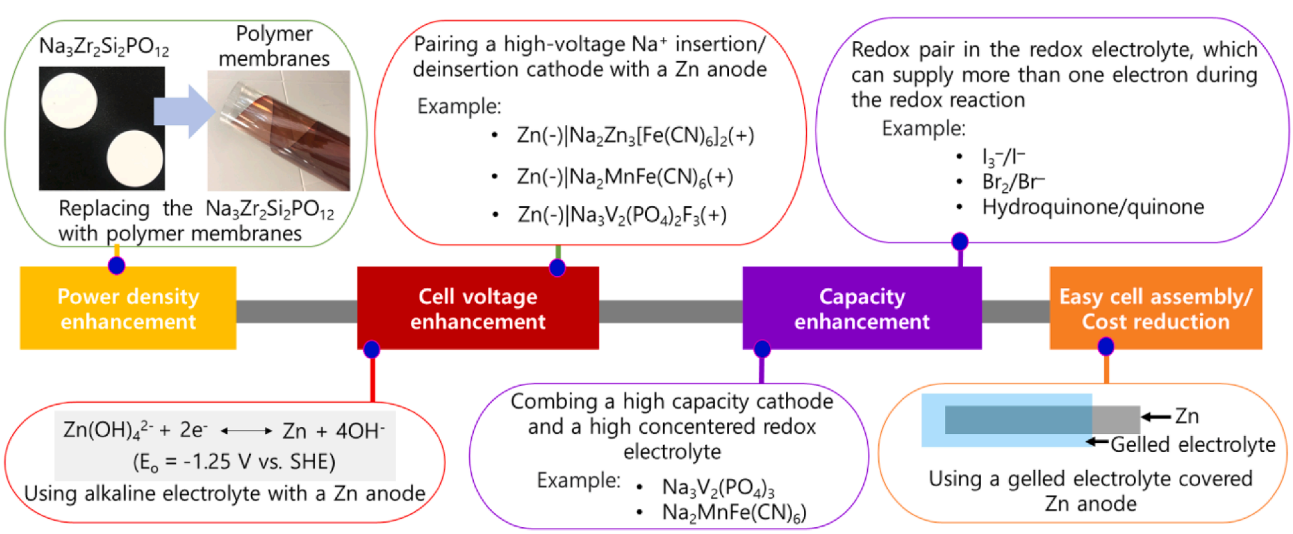

Fig. 6. Future perspective of redox electrolytes used in AHZSIB.

Declaration of Competing Interest

The authors declare that they have no known competing financial interests or personal relationships that could have appeared to influence the work reported in this paper.

Acknowledgement

This work was supported by the 2020 Research Fund (1.200070.01) of UNIST (Ulsan National Institute of Science & Technology). This work was also supported by the National Research Foundation of Korea (NRF) grant funded by the Korean government (MSIT) (No. 2020R1A4A1019568). S.T.S gratefully acknowledges MINECO (Spain) for financial support through the Juan de la Cierva−Incorporación program (Grant No. IJC2018-038426-I). The MFreeB project has received funding from the European Research Council (ERC) under the European Union's Horizon 2020 research and innovation programme (Grant Agreement No. 726217). The results reflect only the authors' view and the Agency is not responsible for any use that may be made of the information they contain.

Appendix A. Supplementary data

Supplementary data to this article can be found online at https://doi.org/10.1016/j.cej.2021.128416.

References

[1] M. Zhang, Z. Huang, Z. Shen, Y. Gong, B. Chi, J. Pu, J. Li, High-performance aqueous rechargeable Li-Ni battery based on Ni(OH)2/NiOOH redox couple with high voltage, Adv. Energy Mater. 7 (2017) 1–7, https://doi.org/10.1002/aenm.201700155.

[2] W. Chen, G. Li, A. Pei, Y. Li, L. Liao, H. Wang, J. Wan, Z. Liang, G. Chen, H. Zhang, J. Wang, Y.i. Cui, A manganese-hydrogen battery with potential for grid-scale energy storage, Nat. Energy. 3 (5) (2018) 428–435, https://doi.org/10.1038/s41560-018-0147-7.

[3] H. Pan, Y. Shao, P. Yan, Y. Cheng, K.S. Han, Z. Nie, C. Wang, J. Yang, X. Li, P. Bhattacharya, K.T. Mueller, J. Liu, Reversible aqueous zinc/manganese oxide energy storage from conversion reactions, Nat. Energy 1 (2016) 16039, https://doi.org/10.1038/nenergy.2016.39.

[4] J. Yan, J. Wang, H. Liu, Z. Bakenov, D. Gosselink, P. Chen, Rechargeable hybrid aqueous batteries, J. Power Sources 216 (2012) 222–226, https://doi.org/10.1016/j.jpowsour.2012.05.063.

[5] L.P. Wang, P.F. Wang, T.S. Wang, Y.X. Yin, Y.G. Guo, C.R. Wang, Prussian blue nanocubes as cathode materials for aqueous Na-Zn hybrid batteries, J. Power Sources 355 (2017) 18–22, https://doi.org/10.1016/j.jpowsour.2017.04.049.

[6] K. Lu, B. Song, J. Zhang, H. Ma, A rechargeable Na-Zn hybrid aqueous battery fabricated with nickel hexacyanoferrate and nanostructured zinc, J. Power Sources 321 (2016) 257–263, https://doi.org/10.1016/j.jpowsour.2016.05.003.

[7] M. Chamoun, T. Gupta, K. Evans-Lutterodt, S. Phadke, S. Biswas, B.J. Hertzberg, A. Kim, T. Luong, D.A. Steingart, Improving the cycle life of a high-rate, high-potential aqueous dual-ion battery using hyper-dendritic zinc and copper hexacyanoferrate, J. Power Sources 305 (2015) 22–29, https://doi.org/10.1016/j.jpowsour.2015.11.065.

[8] C. Liu, Y. Sun, J. Nie, D. Dong, J. Xie, X. Zhao, Stable cycling of a Prussian blue-based Na/Zn hybrid battery in aqueous electrolyte with a wide electrochemical window, New J. Chem. 44 (11) (2020) 4639–4646, https://doi.org/10.1039/C9NJ06024C.

[9] T. Yuan, J. Zhang, X. Pu, Z. Chen, C. Tang, X. Zhang, X. Ai, Y. Huang, H. Yang, Y. Cao, Novel alkaline Zn/Na0.44MnO2 dual-ion battery with a high capacity and long cycle lifespan, ACS Appl. Mater. Interfaces 10 (40) (2018) 34108–34115, https://doi.org/10.1021/acsami.8b0829710.1021/acsami.8b08297.s001.

[10] Y. Zhang, Z. Bakenov, T. Tan, J. Huang, Polyacrylonitrile-nanofiber-based gel polymer electrolyte for novel aqueous sodium-ion battery based on a Na4Mn9O18 cathode and Zn metal anode, Polymers (Basel) 10 (2018) 853, https://doi.org/10.3390/polym10080853.

[11] S. Islam, M.H. Alfaruqi, D.Y. Putro, V. Mathew, S. Kim, J. Jo, S. Kim, Y.-K. Sun, K. Kim, J. Kim, Pyrosynthesis of na3v2 (Po4)3@c cathodes for safe and low-cost aqueous hybrid batteries, ChemSusChem 11 (13) (2018) 2239–2247, https://doi.org/10.1002/cssc.v11.1310.1002/cssc.201800724.

[12] G. Li, Z. Yang, Y. Jiang, W. Zhang, Y. Huang, Hybrid aqueous battery based on Na3V2(PO4)3/C cathode and zinc anode for potential large-scale energy storage, J. Power Sources 308 (2016) 52–57, https://doi.org/10.1016/j.jpowsour.2016.01.058.

[13] P. Hu, T. Zhu, X. Wang, X. Zhou, X. Wei, X. Yao, W. Luo, C. Shi, K.A. Owusu, L. Zhou, L. Mai, Aqueous Zn//Zn(CF 3 SO 3) 2 //Na 3 V 2 (PO 4) 3 batteries with simultaneous Zn 2+ /Na + intercalation/de-intercalation, Nano Energy 58 (2019) 492–498, https://doi.org/10.1016/j.nanoen.2019.01.068.

[14] W. Li, K. Wang, M. Zhou, H. Zhan, S. Cheng, K. Jiang, Advanced low-cost, high-voltage, long-life aqueous hybrid sodium/zinc batteries enabled by a dendrite-free zinc anode and concentrated electrolyte, ACS Appl. Mater. Interfaces 10 (26) (2018) 22059–22066, https://doi.org/10.1021/acsami.8b0408510.1021/acsami.8b04085.s001.

[15] W. Li, K. Wang, S. Cheng, K. Jiang, A long-life aqueous Zn-ion battery based on Na3V2(PO4)2F3 cathode, Energy Storage Mater. 15 (2018) 14–21, https://doi.org/10.1016/j.ensm.2018.03.003.

[16] L. Hu, C. Shi, K. Guo, T. Zhai, H. Li, Y. Wang, Electrochemical double-layer capacitor energized by adding an ambipolar organic redox radical into the electrolyte, Angew. Chem. Int. Ed. 57 (27) (2018) 8214–8218, https://doi.org/10.1002/anie.v57.2710.1002/anie.201804582.

[17] X. Zhang, X. Cui, C.-H. Lu, H. Li, Q. Zhang, C. He, Y. Yang, Conjugated polyimide-coated carbon nanofiber aerogels in a redox electrolyte for binder-free supercapacitors, Chem. Eng. J. 401 (2020) 126031, https://doi.org/10.1016/j.cej.2020.126031.

[18] Y. Wang, Z. Chang, M. Qian, T. Lin, F. Huang, A bridge between battery and supercapacitor for power/energy gap by using dual redox-active ions electrolyte, Chem. Eng. J. 375 (2019) 122054, https://doi.org/10.1016/j.cej.2019.122054.

[19] S.T. Senthilkumar, R.K. Selvan, J.S. Melo, Redox additive/active electrolytes: a novel approach to enhance the performance of supercapacitors, J. Mater. Chem. A 1 (40) (2013) 12386, https://doi.org/10.1039/c3ta11959a.

[20] P. Navalpotro, J. Palma, M. Anderson, R. Marcilla, High performance hybrid supercapacitors by using para-Benzoquinone ionic liquid redox electrolyte, J. Power Sources 306 (2016) 711–717, https://doi.org/10.1016/j.jpowsour.2015.12.103.

[21] Y. Zhu, E. Liu, Z. Luo, T. Hu, T. Liu, Z. Li, Q. Zhao, A hydroquinone redox electrolyte for polyaniline/SnO2 supercapacitors, Electrochim. Acta 118 (2014) 106–111, https://doi.org/10.1016/j.electacta.2013.12.015.

[22] Y. Chen, M. Zhou, Y. Xia, X. Wang, Y. Liu, Y. Yao, H. Zhang, Y. Li, S. Lu, W. Qin, X. Wu, Q. Wang, A stable and high-capacity redox targeting-based electrolyte for aqueous flow batteries, Joule 3 (9) (2019) 2255–2267, https://doi.org/10.1016/j.joule.2019.06.007.

[23] J. Yu, L.i. Fan, R. Yan, M. Zhou, Q. Wang, Redox targeting-based aqueous redox flow lithium battery, ACS Energy Lett. 3 (10) (2018) 2314–2320, https://doi.org/10.1021/acsenergylett.8b0142010.1021/acsenergylett.8b01420.s001.

[24] S.T. Senthilkumar, H. Bae, J. Han, Y. Kim, Enhancing capacity performance by utilizing the redox chemistry of the electrolyte in a dual-electrolyte sodium-ion battery, Angew. Chem. 130 (19) (2018) 5433–5437, https://doi.org/10.1002/ange.v130.1910.1002/ange.201800181.

[25] J. Han, S.M. Hwang, W. Go, S.T. Senthilkumar, D. Jeon, Y. Kim, Development of coin-type cell and engineering of its compartments for rechargeable seawater batteries, J. Power Sources. 374 (2018) 24–30, https://doi.org/10.1016/j.jpowsour.2017.11.022.

[26] S.T. Senthilkumar, J. Han, J. Park, S. Min Hwang, D. Jeon, Y. Kim, Energy efficient Na-aqueous-catholyte redox flow battery, Energy Storage Mater. 12 (2018) 324–330, https://doi.org/10.1016/j.ensm.2017.10.006.

[27] G.K. Veerasubramani, K. Krishnamoorthy, S.J. Kim, Improved electrochemical performances of binder-free CoMoO4 nanoplate arrays@Ni foam electrode using redox additive electrolyte, J. Power Sources 306 (2016) 378–386, https://doi.org/10.1016/j.jpowsour.2015.12.034.

[28] B.o. Hu, C. DeBruler, Z. Rhodes, T.L. Liu, Long-cycling aqueous organic redox flow battery (AORFB) toward sustainable and safe energy storage, J. Am. Chem. Soc. 139 (3) (2017) 1207–1214, https://doi.org/10.1021/jacs.6b1098410.1021/jacs.6b10984.s001.

[29] T. Liu, X. Wei, Z. Nie, V. Sprenkle, W. Wang, A total organic aqueous redox flow battery employing a low cost and sustainable methyl viologen anolyte and 4-HO-TEMPO catholyte, Adv. Energy Mater. 6 (3) (2016) 1501449, https://doi.org/10.1002/aenm.201501449.

[30] C. Liu, L. Shaw, A high capacity, room temperature, hybrid flow battery consisting of liquid Na-Cs anode and aqueous NaI catholyte, Batteries 4 (2018) 60, https://doi.org/10.3390/batteries4040060.

[31] Y. Ding, G. Yu, A. Bio-Inspired, Heavy-metal-free, dual-electrolyte liquid battery towards sustainable energy storage, Angew. Chem. Int. Ed. 55 (2016) 4772–4776, https://doi.org/10.1002/anie.201600705.

[32] C.D. Wessells, S.V. Peddada, R.A. Huggins, Y.i. Cui, Nickel hexacyanoferrate nanoparticle electrodes for aqueous sodium and potassium ion batteries, Nano Lett. 11 (12) (2011) 5421–5425, https://doi.org/10.1021/nl203193q.

[33] W. Li, F. Zhang, X. Xiang, X. Zhang, High-efficiency Na-storage performance of a nickel-based ferricyanide cathode in high-concentration electrolytes for aqueous sodium-ion batteries, ChemElectroChem 4 (11) (2017) 2870–2876, https://doi.org/10.1002/celc.201700776.

[34] F. Ma, X. Yuan, T. Xu, S. Zhou, X. Xiong, Q.i. Zhou, N. Yu, J. Ye, Y. Wu, T. van Ree, A high-quality monoclinic nickel hexacyanoferrate for aqueous zinc-sodium hybrid batteries, Energy Fuels 34 (10) (2020) 13104–13110, https://doi.org/10.1021/acs.energyfuels.0c02349.

[35] W. Li, H.-C. Fu, Y. Zhao, J.-H. He, S. Jin, 14.1% efficient monolithically integrated solar flow battery, Chem 4 (11) (2018) 2644–2657, https://doi.org/10.1016/j.chempr.2018.08.023.

[36] K.e. Gong, F. Xu, J.B. Grunewald, X. Ma, Y. Zhao, S. Gu, Y. Yan, All-soluble all-iron aqueous redox-flow battery, ACS Energy Lett. 1 (1) (2016) 89–93, https://doi.org/10.1021/acsenergylett.6b0004910.1021/acsenergylett.6b00049.s001.

[37] S. Kaipannan, S. Marappan, Fabrication of 9.6 V high-performance asymmetric supercapacitors stack based on nickel hexacyanoferrate-derived Ni(OH)2

nanosheets and bio-derived activated carbon, Sci. Rep. 9 (2019) 1104, https://doi.org/10.1038/s41598-018-37566-8.
[38] L. Shen, Y.u. Jiang, Y. Liu, J. Ma, T. Sun, N. Zhu, High-stability monoclinic nickel hexacyanoferrate cathode materials for ultrafast aqueous sodium ion battery, Chem. Eng. J. 388 (2020) 124228, https://doi.org/10.1016/j.cej.2020.124228.
[39] F. Chen, J. Wang, C. Feng, J. Ma, T. David Waite, Low energy consumption and mechanism study of redox flow desalination, Chem. Eng. J. 401 (2020) 126111, https://doi.org/10.1016/j.cej.2020.126111.
[40] A. Orita, M.G. Verde, M. Sakai, Y.S. Meng, The impact of pH on side reactions for aqueous redox flow batteries based on nitroxyl radical compounds, J. Power Sources 321 (2016) 126–134, https://doi.org/10.1016/j.jpowsour.2016.04.136.
[41] X. Wu, Y. Cao, X. Ai, J. Qian, H. Yang, A low-cost and environmentally benign aqueous rechargeable sodium-ion battery based on NaTi2(PO4)3–Na2NiFe(CN)6 intercalation chemistry, Electrochem. Commun. 31 (2013) 145–148, https://doi.org/10.1016/j.elecom.2013.03.013.
[42] S.T. Senthilkumar, M. Abirami, J. Kim, W. Go, S.M. Hwang, Y. Kim, Sodium-ion hybrid electrolyte battery for sustainable energy storage applications, J. Power Sources 341 (2017) 404–410, https://doi.org/10.1016/j.jpowsour.2016.12.015.
[43] Y. Chen, H.J. Woo, M. Rizwan, R.B. Yahya, D. Cui, D. Luo, L. Chen, A.K.M. Arof, F. Wang, Nanoscale morphology control of na-rich prussian blue cathode materials for sodium ion batteries with good thermal stability, ACS Appl. Energy Mater. 2 (12) (2019) 8570–8579, https://doi.org/10.1021/acsaem.9b0149110.1021/acsaem.9b01491.s001.
[44] Z. Chang, D. Henkensmeier, R. Chen, Shifting redox potential of nitroxyl radical by introducing an imidazolium substituent and its use in aqueous flow batteries, J. Power Sources 418 (2019) 11–16, https://doi.org/10.1016/j.jpowsour.2019.02.028.
[45] V. Medabalmi, M. Sundararajan, V. Singh, M.-H. Baik, H.R. Byon, Naphthalene diimide as a two-electron anolyte for aqueous and neutral pH redox flow batteries, J. Mater. Chem. A 8 (22) (2020) 11218–11223, https://doi.org/10.1039/D0TA01160F.
[46] C. Yang, X. Liu, K. Yang, Y. Lai, K. Zhang, Z. Tian, Effects of hydrogen bubbles on deformation of zinc anodes at high depth of discharge, J. Solid State Electrochem. (2020) 2–7, https://doi.org/10.1007/s10008-020-04838-1.
[47] J. Zhang, G. Jiang, P. Xu, A. Ghorbani Kashkooli, M. Mousavi, A. Yu, Z. Chen, An all-aqueous redox flow battery with unprecedented energy density, Energy Environ. Sci. 11 (8) (2018) 2010–2015, https://doi.org/10.1039/C8EE00686E.
[48] Z. Yuan, Y. Duan, T. Liu, H. Zhang, X. Li, Toward a low-cost alkaline zinc-iron flow battery with a polybenzimidazole custom membrane for stationary energy storage, IScience 3 (2018) 40–49, https://doi.org/10.1016/j.isci.2018.04.006.
[49] L. Zhang, L. Chen, X. Zhou, Z. Liu, Morphology-dependent electrochemical performance of zinc hexacyanoferrate cathode for zinc-ion battery, Sci. Rep. 5 (2015) 18263, https://doi.org/10.1038/srep18263.
[50] Z. Hou, X. Zhang, X. Li, Y. Zhu, J. Liang, Y. Qian, Surfactant widens the electrochemical window of an aqueous electrolyte for better rechargeable aqueous sodium/zinc battery, J. Mater. Chem. A 5 (2) (2017) 730–738, https://doi.org/10.1039/C6TA08736A.
[51] B. Li, Z. Nie, M. Vijayakumar, G. Li, J. Liu, V. Sprenkle, W. Wang, Ambipolar zinc-polyiodide electrolyte for a high-energy density aqueous redox flow battery, Nat. Commun. 6 (2015) 6303, https://doi.org/10.1038/ncomms7303.
[52] G.G. Yadav, D. Turney, J. Huang, X. Wei, S. Banerjee, Breaking the 2 V barrier in aqueous zinc chemistry: creating 2.45 and 2.8 V MnO 2 –Zn aqueous batteries, ACS Energy Lett. 4 (9) (2019) 2144–2146, https://doi.org/10.1021/acsenergylett.9b01643.